Soil Dynamics and Earthquake Engineering 209 (2026) 110446

Contents lists available at ScienceDirect

Soil Dynamics and Earthquake Engineering

journal homepage: www.elsevier.com/locate/soildyn

Predictive tools for seismic fragility and damage probability maps of bridges with reinforced concrete circular piers

R. Martini, L. Tentella, A. Brunetti, S. Carbonari *, F. Gara

Dept. of Construction, Civil Engineering and Architecture (DICEA), Università Politecnica Delle Marche, Ancona, Italy

ARTICLE INFO

Keywords:
Circular bridge piers
Seismic fragility curves
Multivariate regression models
Artificial neural networks
Damage maps

ABSTRACT

This paper presents a comprehensive numerical investigation into the seismic fragility of circular reinforced concrete bridge piers, which represent a widely adopted structural typology due to their structural isotropy and hydraulic efficiency. Despite their prevalence, there is a lack of tailored fragility functions that systematically account for the specific geometric and mechanical parameters governing their seismic response. To address this gap, a parametric study was conducted on a wide range of pier configurations, varying the height-to-diameter ratio, the normalized axial load, the longitudinal reinforcement ratio, and the transverse reinforcement volumetric ratio. Nonlinear time-history analyses were performed using multiple stripe analysis to derive fragility curves for five distinct damage states, ranging from initial yielding to collapse, including both ductile and brittle failure mechanisms. The role of the parameters on the seismic response is studied by systematically addressing the sensitivity of fragility parameters to the investigated input variables. Furthermore, simplified prediction tools are proposed, including multivariate regression models and artificial neural networks, to estimate fragility parameters without the need for computationally expensive nonlinear analyses. Finally, the applicability of these tools in the framework of the post-earthquake emergency management is demonstrated.

1. Introduction

Piers play a crucial role in the seismic performance of bridges, acting as the primary load-carrying and energy-dissipating components during earthquake events. Evidences from past earthquakes, such as the 1971 San Fernando, 1994 Northridge, 1995 Kobe, and 1999 Chi-Chi earthquakes, have demonstrated that severe damage or collapse of Reinforced Concrete (RC) bridge piers are responsible for high direct and indirect economic losses, as a consequence of the repairing costs and the overall disruption of transportation networks [1,2]. Consequently, accurate assessment of the seismic vulnerability of RC piers has become a central issue in performance-based earthquake engineering and infrastructure resilience.

Seismic fragility analysis has emerged as an effective probabilistic framework for quantifying the likelihood that a structural component or system will reach or exceed predefined damage states under increasing levels of seismic intensity [3,4]. Fragility curves can explicitly incorporate uncertainties related to material properties, geometry, modelling assumptions, and seismic demand, and they form the backbone of modern performance-based assessment methodologies such as HAZUS and FEMA P-58 [5]. However, among the previous ones, uncertainties related to the seismic actions are those governing the variability of structural response [6,7].

In the context of bridges, fragility analysis has been extensively applied to estimate damage probabilities, support network-level loss assessment, and guide retrofit prioritization [8,9]. Early and widely adopted fragility functions for bridge piers were obtained from incremental dynamic analysis (IDA) and probabilistic seismic demand modelling, where nonlinear time-history analyses are used to estimate structural responses across suites of ground motions. These methods form the basis of many analytical fragility studies that foresee a complete modelling of the bridge components and the relevant inelastic mechanisms under increasing seismic demand, and fit statistical fragility functions for defined limit states. However, recent research highlights the importance of deriving component-level fragilities specifically (e.g., for piers, bearings, decks) [10] because system fragilities often mask the vulnerability contributions of individual elements. For example, studies demonstrate that the pier may govern failure for simply supported bridges while bearings or superstructure may have a relevance in case of multi-span bridges [11].

* Corresponding author.
E-mail address: s.carbonari@univpm.it (S. Carbonari).

https://doi.org/10.1016/j.soildyn.2026.110446
Received 7 May 2026; Received in revised form 29 May 2026; Accepted 3 June 2026
Available online 26 June 2026

With focus on component-level fragilities, the research has given particular attention to piers. Among the various pier configurations, circular reinforced concrete piers are widely adopted in modern bridge construction due to their geometric symmetry, confinement efficiency, hydraulic compatibility, and favourable ductility characteristics under cyclic loading [2,12,13]. The circular cross-section provides uniform stiffness and strength in all horizontal directions, while providing superior hydraulic compatibility due to their smooth and symmetric geometry, which reduces flow disturbance and turbulence. This results in more uniform flow patterns and lower head losses and scour potential compared with non-circular pier geometries.

Circular reinforced concrete piers deserve focused investigation due to their widespread application in bridge construction and their favourable seismic performance characteristics. Although no official statistics are available defining the percentage of bridges in Italy with circular cross-section piers, it can be stated that in reinforced concrete bridges built in the post-war period (1950s–1970s) the most common pier shapes are circular and rectangular. A local assessment carried out along two state roads in central Italy found that, on a bridge stock of 91 bridges, the percentage of bridges with circular piers is approximately 40% [14,15]. Another study, revealed that on a stock of 485 bridges in Italy, the 20% is characterized by circular piers [16].

Despite these advantages, only few works, to the Authors' knowledge, concentrated on the seismic fragility of circular piers. A core advancement in the seismic assessment of circular reinforced concrete piers is the recent work by Miano et al. [17], which directly addresses the development of tailored fragility curves for circular piers in simply supported bridges. In this study, fragility curves are generated using both the capacity spectrum method and response spectrum analysis applied to an analytical model representative of a typical single-span RC bridge with circular piers. A comprehensive parametric study explores the influence of key geometric (pier diameter and height, span length) and mechanical (concrete strength, reinforcement yield strength, transverse reinforcement ratio) properties on seismic capacity. The authors introduce a multilinear regression model that provides predictive estimates of the median seismic performance (e.g., PGA at damage state thresholds) as a function of these properties. Their results highlight the relative conservatism of linear methods compared to nonlinear approaches and demonstrate how confinement provided by transverse reinforcement affects pier fragility curves across defined damage states. However, comprehensive dynamic nonlinear time history analyses are not performed, and fragility parameters are only provided in terms median capacity by performing simplified nonlinear static and response spectrum analysis. In parallel [18–20], expand fragility analysis into the context of deterioration due to corrosion. This study integrates a novel computer vision algorithm to classify corrosion severity on circular bridge piers from photographic surveys, and couples this with probabilistic seismic fragility analysis. The framework quantifies the effect of corrosion induced strength and stiffness degradation on seismic vulnerability and risk metrics. While not limited to fragility curves in the classical analytical sense, it extends the fragility approach to account for condition dependent uncertainty, reflecting real world deterioration that influences damage probabilities. Anyway, the work focuses on the fragility of a specific bridge providing a framework which is not suitable for addressing the fragility of bridge classes to be used for the risk assessment at territorial scale.

Retrofit focused fragility studies, such as the investigation of RC jacketing on circular piers, provide additional insights into how structural strengthening alters seismic vulnerability. In this context, research on fragility curves for single column bridges retrofitted with RC jackets demonstrates that jacketing increases base shear capacity and systematically reduces the probability of reaching high damage states under seismic demand. Fragility curves are developed for multiple limit states (e.g., slight, moderate, severe, collapse) as a function of peak ground acceleration, showing how retrofit parameters such as jacket thickness and additional reinforcement influence vulnerabilities. Although these retrofitting studies are broader than purely geometric circular piers, they underscore the dependency of fragility behavior on intervention strategies and offer empirical relationships that can support tailored fragility modelling [21,22].

Overall, the literature illustrates a growing trend in seismic fragility research toward geometry specific, condition informed, and retrofit sensitive fragility functions. While classical fragility frameworks applied to bridges have been widely applied to generic infrastructures, works tailored to specific RC cross-sections, through detailed analytical modelling and regression based predictive tools, are limited in the literature. Considering these represent an important step in enhancing the accuracy and applicability of fragility functions for performance based seismic assessment and risk management of bridge infrastructure, further studies are desirable in the future.

This paper addresses the lack of tailored fragility functions by focusing on the seismic performance of circular RC bridge piers. Section 2 presents the research framework and the analysis methodology, which involves the use of nonlinear time-history analyses to derive fragility curves fitted with lognormal distributions through the maximum likelihood estimation method, while accounting for uncertainties in the seismic input.

In Section 3, a comprehensive parametric study is carried out on a wide range of pier configurations, varying the main mechanical and geometrical properties that influence the seismic response, including the height-to-diameter ratio, the normalized axial load, the longitudinal reinforcement ratio, and the volumetric ratio of transverse reinforcement [23]. The same section also defines the parameters adopted for the fragility analyses, such as bridge performance levels, Engineering Demand Parameters (EDPs), and Intensity Measure (IM) levels.

Section 4 provides a critical discussion of the fragility results, highlighting the relevance of the selected parameters and identifying the corresponding bridge classes. In addition, regression-based closed-form expressions are derived to estimate the parameters of the lognormal fragility curves as functions of the geometrical and mechanical characteristics of the bridges. For the same purpose, a neural network model is also developed to improve the prediction of fragility parameters.

Finally, Section 5 demonstrates the applicability of the proposed tools through the derivation of conditional damage probability maps for selected bridge categories based on site-specific hazard maps. These damage maps can play a key role in post-earthquake decision-making and emergency management. The main findings of the study are summarized in the concluding section.

2. Research framework and analysis methodology

The seismic fragility of reinforced concrete, steel and steel-concrete composite bridges is mainly dominated by failure mechanisms that involve support devices and piers, while the deck is usually less sensitive to seismic induced damage. Indeed, the in-plane response of the deck of such bridges can rely on a considerably high strength of the slab triggered by the significant effective depths of the cross-section and the amount of longitudinal reinforcement ratios that are in the range of 1%-2%. As for the support devices, it should be mentioned that since 1991 [24], in Italy the seismic design of deck restraints is performed considering a safety factor of 1.4. According to above considerations, the paper focuses on the ductile and fragile failure mechanisms associated with the pier response and the seismic response is assessed by assuming a cantilever static scheme. Although its simplicity, the modelling approach is largely adopted in practical design of bridges because it may be assumed as representative of different structural configurations. Indeed, the cantilever scheme with a head masse of the tributary deck is representative of the overall longitudinal and transverse dynamics of bridges with simply supported decks (about 77%, on a sample of 447 bridges investigated by the FABRE Consortium) [25], as well as of the transverse dynamics of multi-span bridges (about 12%, on the same sample), provided that piers have similar height, and dual-load path mechanisms involving the transverse resistance of the abutment are excluded. In case of dual-load path systems, the adopted simple model may be representative of the transverse response of inner piers, where the boundary effects due to the abutment contribution can be neglected. Finally, the approach can be also suitable for modelling the longitudinal dynamic response of multi-span bridges if piers have similar height and absorb the longitudinal seismic actions through dynamic restraint devices (e.g. shock transmitters).

In addition, the circular cross-section represents a widely adopted typology for bridge piers in Italy due to its structural isotropy, which ensures a uniform seismic response regardless of the direction of the earthquake, and hydraulic compatibility, which reduces flow resistance and turbulence, effectively mitigating the risk of bridge scour at the foundations. Furthermore, the use of standardized steel formwork allows for a highly efficient and cost-effective construction process, making it the preferred choice for large-scale infrastructural projects and viaducts.

A concentrated plasticity model developed in OpenSees [26] is used for the pier by considering a zero-length nonlinear rotational spring at the pier base to simulate the elastic and plastic contribution to the pier deflection due to the inelastic section (Fig. 1).

In addition, a rigid link is included above the nonlinear one, conventionally equal to the plastic hinge length, which ensures a proper implementation of the Takeda hysteretic law [27]. The moment-rotation relationship is calibrated so that the pier head displacement obtained from the concentrated plasticity model under a head lateral load matches the one obtained by integrating a linear elastic curvature and an equivalent distributed plastic curvature over the hinge length. The yielding and ultimate hinge rotations are provided by the following expressions:

$$\vartheta_y = \frac{M_y}{3EJh^2}\left[h^3 - (h - L_p)^3\right] \tag{1}$$

$$\vartheta_u = \frac{M_y}{3EJh^2}\left[h^3 - (h - L_p)^3\right] + \left(\phi_u - \frac{M_u}{EJ}\right)L_p\left[1 - \frac{L_p}{2h}\right] \tag{2}$$

where, h is the pier height, EJ is the cracked flexural stiffness of the cross-section, ϕ_y and ϕ_u are the yielding and ultimate curvatures of the base pier cross-section, ϑ_y and ϑ_u are the yielding and ultimate rotations of the zero-length plastic hinge, respectively, associated to the yielding and ultimate bending moments M_y and M_u, respectively. The yielding and ultimate curvatures usually refer to a bilinear approximation of the bending moment-curvature curve obtained from a nonlinear cross-sectional analysis [13]. In this work, the sectional analyses are carried out in OpenSees by adopting a fiber cross-section modelling, distinguishing between the unconfined and confined concrete regions. The cross-section discretization is obtained by exploiting polar symmetry and generating 3600 and 240 fibers for confined and unconfined concrete regions, respectively. Concrete is modeled using the constitutive law proposed by Popovics [28], adopting different values of compressive strength and ultimate strain for the confined and unconfined materials, computed using the generalized formulation proposed by Mander [12], with reference to the coefficients suggested by Chang and Mander [29]. Rebars are modeled using the constitutive law proposed by Menegotto and Pinto [30]. The cross-section is assigned to a zero-length element, and the moment-curvature relationship is obtained with a displacement controlled nonlinear analysis, by imposing an incremental relative rotation between the two nodes of the element.

As for the global modelling, a sufficiently refined mesh (10 finite elements) is adopted for the elastic pier section to account for the distribution of the mass and to capture minor effects due to higher modes, which may be relevant for tall piers. Furthermore, a 5% tangent stiffness proportional viscous damping is applied to both models [13].

The seismic fragility assessment is carried out through nonlinear dynamic time-history analyses assuming the pier head displacement as the EDP, and taking advantage of the Multiple Stripe Analysis (MSA) methodology [31]. For each IM, a sufficient number of real scaled seismic events are considered in order to obtain a sound statistical representation of the EDP. Different performance levels for the pier are established in terms of EDP to define Damage States (DSs) associated to both ductile and fragile mechanisms. Finally, the Cumulative Density Functions (CDFs), namely the fragility curves for each DS, are classically obtained adopting a lognormal distribution whose parameters are calibrated through the Maximum Likelihood Estimation (MLE) method [31]. Thus, the fragility curve for the i-th damage state (DS_i) can be expressed through

$$P(DS_i|IM = im) = \Phi\left(\frac{ln(im) - ln(\theta)}{\beta}\right) \tag{3}$$

where im is independent variable, Φ is the CDF, and θ and β are the median value and standard deviation, respectively, of the lognormal distribution. It is worth noting that θ represents the value of the IM at

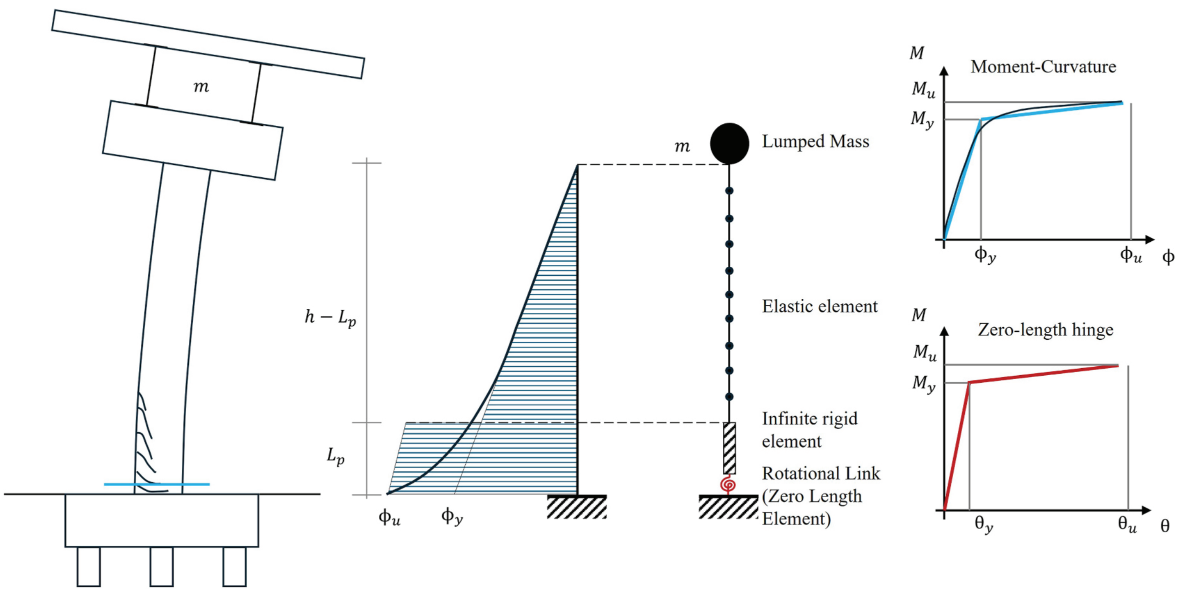

Fig. 1. Scheme of numerical model of the bridge pier.

which there is a 50% probability of exceeding the defined DS, while β, commonly referred to as dispersion, quantifies the total uncertainty associated with the damage prediction.

3. Definition of the parametric investigation

As recognised in the literature, the structural behavior of circular piers is strongly influenced by parameters such as slenderness, axial load, and reinforcement ratios. In this work, the following nondimensional parameters are selected to generate a wide number of case studies according to a parametric scheme: *i*) the slenderness ratio h/D, defined as the ratio between the pier height h and diameter D; *ii*) the normalized axial load ν, defined as the ratio between the axial force acting on the pier at seismic condition (directly related to the deck tributary mass) and the maximum compressive capacity of the concrete cross-section; *iii*) the longitudinal reinforcement ratio ρ_l, expressing the percentage of total longitudinal steel area over the gross concrete cross-section area, and *iv*) the volumetric confinement ratio ω, defined as the ratio between the volume of transverse confinement reinforcement and the volume of the confined concrete core.

Above parameters are varied in order to cover a wide range of real bridges; in detail, upper and lower bounds are selected not only consistently with data available in the literature [32,33], but also with reference to recommendations and practice rules reported in the historic Italian code [34]. Table 1 collects values assigned to the different parameters. For each parameter, three intermediate values, in addition to the boundary ones, are defined balancing the computational cost with the need of obtaining a dataset of statistical significance. Combination of the parameters generates a total of 625 analysis cases, which is deemed suitable for a statistical investigation.

Five performance levels of the piers are defined in terms of curvature thresholds for the base cross-section, following literature [35] and code considerations [36], with the aim of capturing the initial yielding of the reinforcements, the nominal yielding of the cross-section, and the collapse, associated to both ductile and fragile mechanisms. Thresholds are associated to different Damage States (DSs) attained when specific limits of the concrete strain ε_c and of the steel strain ε_s are reached, as well as when the 10% reduction of the maximum bending moment or a shear force higher than the resisting one is observed. The performance for the different DSs are reported in Table 2: DS1 represents the elastic limit state; DS2 corresponds to moderate damage typically characterized by concrete spalling, associated to the curvature corresponding to 0.4% strain for concrete or 1.5% strain for steel, whichever occurs first [13]; DS3 denotes a significant damage associated to a conventional Life Safety Limit state, attained for a curvature equal to 0.7 the ultimate one, as conventionally assumed in modern seismic codes [36,37]; finally, DS4 is representative of the collapse, occurring at a 10% reduction of the maximum bending moment, or at a steel strain of 7.5% [37]. To account for possible brittle mechanisms, the shear capacity of the elements is evaluated using the approach proposed by Priestley et al. [13], which accounts for the ductility-related degradation of the shear strength. In detail, the shear strength is determined as the combination of three contributions: the ductility sensitive concrete contribution, provided by the aggregate interlock, the compression zone, and the dowel action, the transverse reinforcement contribution, and the axial load contribution, which is evaluated as the horizontal component of an inclined compression strut developed between the centers of the compression zones at the column ends. Provided that the base bending moment can be expressed as a function of the shear force, according to the cantilever scheme of the pier, the comparison between the flexural capacity curve and the shear strength allows to characterize the ductile or brittle behavior of the pier. When brittle failure occurs before the complete formation of a ductile mechanism, the corresponding performance limit is identified and defined as DS5 (Fig. 2).

Table 1
Variability of parameters adopted in the analyses.

h/D [-]	ν [%]	ρ_l [%]	ω [-]
3	4	0.3	0.5
4.5	6	0.6	3
6	8	0.9	6
7.5	10	1.2	9
9	12	1.5	12

Table 2
Definition of DS and curvature limits.

Damage State	Curvature [m^{-1}]	EDP
DS1	$\chi_1 = \varphi_y$	d_1
DS2	$\chi_2 = \min(\varphi\text{: } \varepsilon_c > 0.004,\ \chi\text{: } \varepsilon_s \geq 0.015)$	d_2
DS3	$\chi_3 = 0.7\chi_4$	d_3
DS4	$\chi_4 = \min(\varphi\text{: } \Delta M = 0.1M_{max},\ \chi\text{: } \varepsilon_s \geq 0.075)$	d_4
DS5	$\chi_5 = (\chi\text{: } V{=}V_R)$	d_5

3.1. Fragility analyses

The fragility of each pier (of the 625 investigated) with respect to the selected DSs was evaluated using the well-established Multiple Stripe Analysis (MSA) methodology [31]. Consistently with the paper aim, which focuses on the fragility of the selected structural taxonomy, the structural capacity was decoupled from the site-specific hazard, by defining the seismic input through a series of discrete Intensity Measure (IM) levels, adopting the Peak Ground Acceleration (PGA) as the reference parameter [38]. For each stripe, a suite of ground motion records was selected and scaled so that their mean PGA matches the target IM. In addition to the PGA, the spectral shape of the ground motion records was also explicitly considered to ensure consistency of the seismic demand with the conventional code hazard in terms of frequency content and spectral accelerations. The adopted spectral shape was defined according to the Eurocode 8 [23] Type 1 elastic response spectrum for Ground Type A, and the compatibility of the average spectrum of the records set is evaluated within the range −30% and +30% of the target spectral ordinates in the period range 0.15-2 s, in which all the fundamental periods of the investigated bridges fall. Using a Type A spectrum as a reference shape provides a standardized, site-independent hazard baseline, effectively isolating the structural vulnerability from local stratigraphic amplification effects. The dual-parameter characterization of seismic action mitigates the risk of spectral bias, ensuring that the scaled records overall exhibit a frequency content compatible with the code hazard, while providing a robust statistical sampling of the

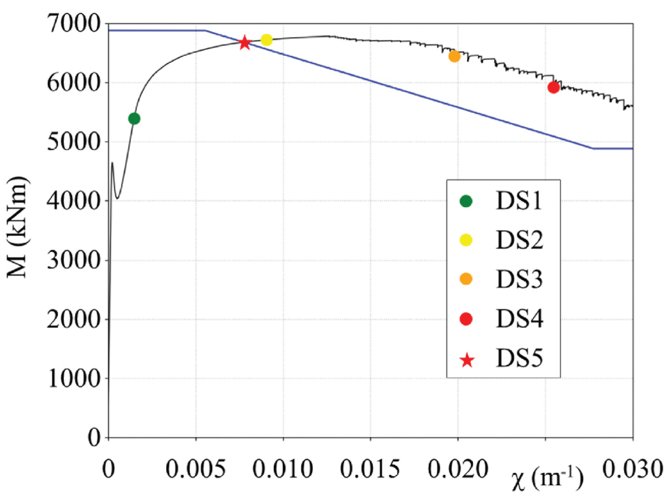

Fig. 2. Curvature thresholds definition in the moment-curvature diagram for the pier base cross-section (h/D = 3, ν = 4%, ρ_l = 0.3%, ω = 0.5%).

record-to-record variability, capturing the influence of different frequency contents and durations on the dynamic response of the structural class. The approach tends to mitigate the risk of overestimating or underestimating structural damage, which could occur if the scaled records exhibited spectral ordinates significantly divergent from those expected for the reference hazard. Integrating spectral shape considerations thus enhances the sufficiency and efficiency of the chosen IM, leading to more reliable fragility functions for the structural population. By incrementally increasing the IM levels according to the reference spectral shape, the evolution of the Engineering Demand Parameters (EDP) was monitored, providing a robust statistical basis for the calibration of the log-normal fragility functions.

Operatively, 16 IM values were selected, ranging from 0.08 to 0.9 g (Fig. 3a) and, for each IM level, 20 natural spectrum-compatible accelerograms were selected (Fig. 3b), using the “Select & Match” software developed by Manfredi et al. [39]. For a medium seismicity site, characterized by a PGA of 0.2 g associated to a probability of exceedance of 10% in 50 years, the selected IMs cover a range of return periods from about 30 to 35000 years. The total number of analyses performed for each case of the parametric study is therefore 320 nonlinear dynamic analyses, for an overall number of 200000 applications for the entire bridge stock. Consistently with the monitored EDP, the attainment of the DSs is expressed in terms of deck displacement d in order to identify the selected performance levels.

4. Seismic fragility of circular r.c. piers

To provide an initial insight into the analysis results obtained for the 625 bridge piers across all 200000 applications, Fig. 4 presents the fragility curves for two of the investigated damage states (DSs): the first yielding of the reinforcement (DS1) and the conventional attainment of the life-safety limit state (DS3), defined as a pier base cross-section curvature equal to approximately 0.7 times the ultimate curvature. Specifically, the fragility curves for DS1 and DS3 are shown in separate rows for three selected h/D ratios (3, 6, and 9). Within each row, the same curves reflect the variability of the remaining parameters (ν, ρ_l, and ω) and are presented across three columns. Each column, reporting the same curves, highlights the influence of one parameter by using a gradient color scale to describe the variation of the considered parameter, thereby providing a preliminary assessment of the contribution of each parameter to pier fragility.

As for DS1, an overall fragile behavior is observed for all the h/D ratios (high slopes of the curves) as well as a more pronounced dependency of the fragility on the parameter ν, which affects not only the initial axial strain of rc and steel fibers of the cross-section but most importantly the tributary mass of the deck and consequently the fundamental period of the bridge. For h/D equal to 3 and 6, by increasing ν, curves move towards lower IMs while for h/D equal to 9, by increasing ν, curves move towards higher IMs and the fragility tends to slightly reduce. These phenomena are consistent with the expected increase in structural period as ν increases, and the corresponding effects on spectral ordinates, which tend to increase for short-period structures and decrease for long-period ones. The fragility reduction observed for h/D = 9 and for high values of ν may be due to the record-to-record variability, namely to an increase of the spectral ordinates dispersion at the bridge fundamental period resulting from the set of records. Fragility curves for DS1 are less affected by the longitudinal reinforcement ratio variability, consistently with experimental and literature evidences [13]. Finally, as expected, the transverse reinforcement ratio ω does not affect the pier first yielding.

The behavior with respect to DS3 is less fragile than DS1, as highlighted with the slope reduction of the curves, even if for h/D = 3 relatively high slopes are observed by increasing ν, and by reducing the transverse reinforcement ratio ω, as a consequence of the reduced confinement effects of concrete. Overall, fragility is sensitive to all the parameters (ν, ρ_l, and ω): for all the h/D ratios, by reducing ν, fragility curves move towards higher IMs and the slopes reduce consistently with the well-known effects of the axial force on the ductility capacity of rc members. This behavior is less evident for h/D = 9, for which, in addition to the fragility curves shift towards higher IMs, also an increase of the slope is observed. Furthermore, by increasing the longitudinal and transverse reinforcement ratios ρ_l and ω, fragility functions generally move towards higher IMs and slopes reduce, highlighting a reduction of the DS fragility; this is particularly evident for h/D ratios equals to 3 and 6, while less pronounced for h/D = 9. Indeed, for this h/D ratio, the increment of the reinforcement ratios, in conjunction with the reduction of the axial force ratio produces a shift of the fragilities towards higher IMs, which is however associated to an increase of the fragility; as in the previous case, this outcome may have an input-related nature.

Above considerations support the need for a deeper and systematic understanding of the role of each parameter of the investigation into the seismic fragility of the piers, with respect to the different selected performances (i.e. DSs).

4.1. Role of the varying parameter on the seismic fragility

The impact of the input parameters $\boldsymbol{p} = [h/\mathrm{D} \quad \nu \quad \rho_l \quad \omega]$ on the fragility functions output parameters $\boldsymbol{q} = [\theta \quad \beta]$ for the generic DS, is studied using the Kernel Density Estimation (KDE) approach. Unlike traditional frequentist approaches that rely on discrete histograms, KDE provides a non-parametric, continuous estimation of the probability density function (PDF), allowing for a more nuanced interpretation of the response surface and its sensitivities. Specifically, the i-th stochastic parameters q_i is treated as a random variable derived from n independent parametric simulations, and the KDE of its density function, denoted as $P(q_i)$, is defined as the superposition of Gaussian kernel functions centred at each observed data point $q_{i,k}$ ($k = 1,\ldots,n$), and the bandwidth is selected automatically according to Scott's rule [40]:

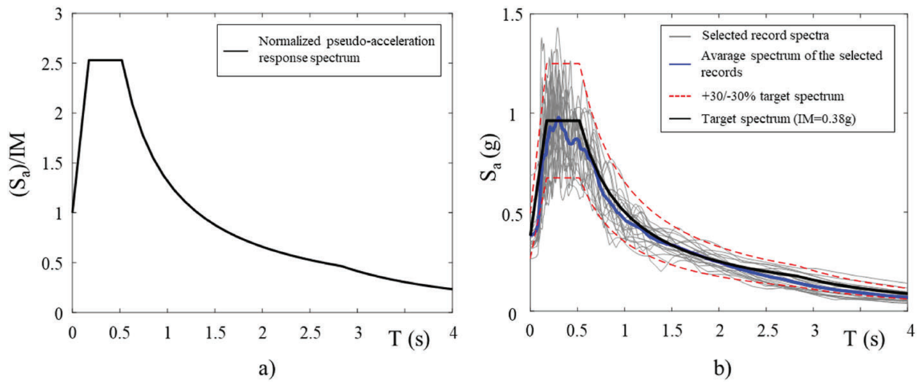

Fig. 3. a) Normalized pseudo-acceleration response spectrum, b) Comparison of selected earthquake response spectra with reference hazard for IM = 0.38 g.

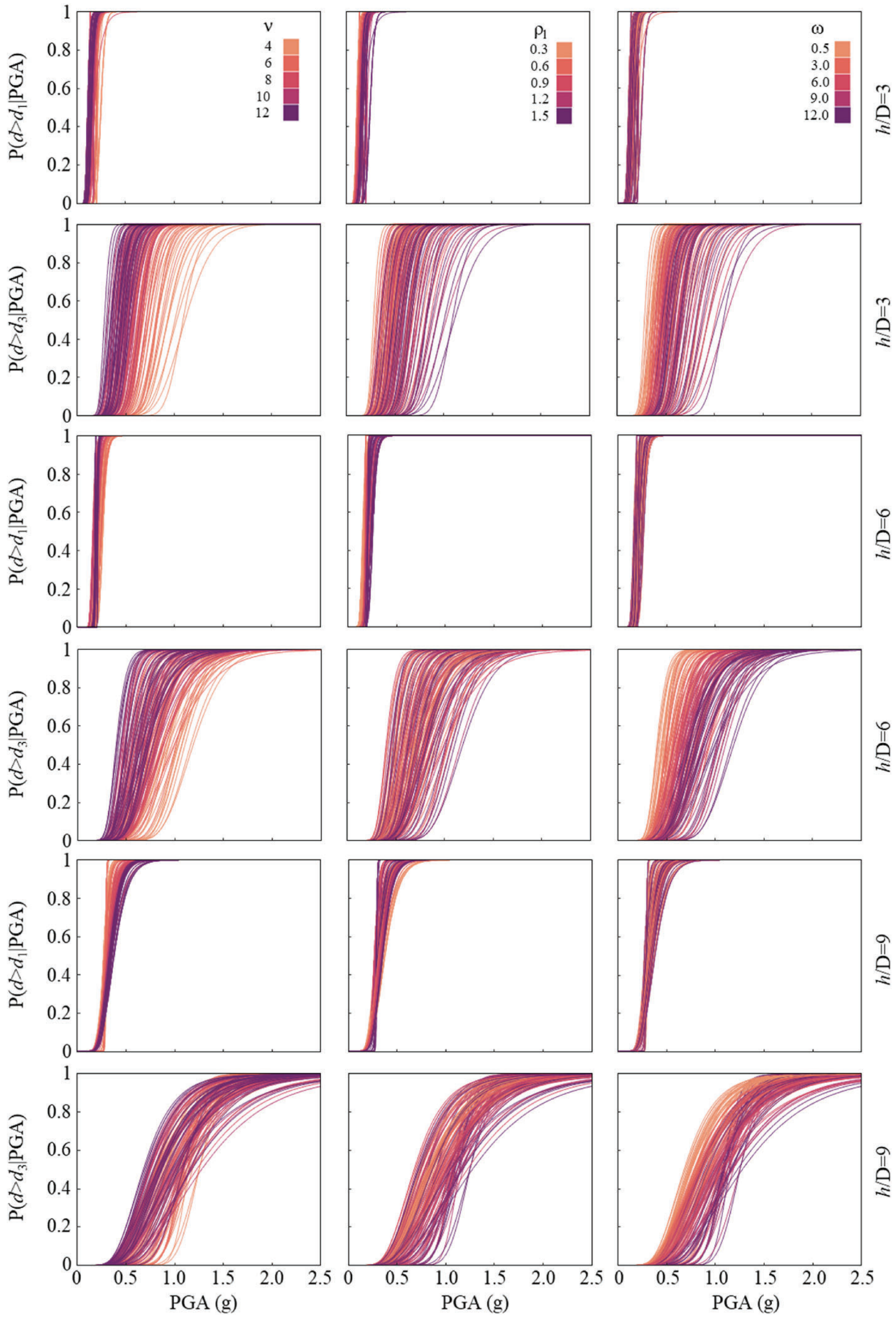

Fig. 4. Fragility curves for DS1 and DS3 obtained from the analyses for $h/\mathrm{D} = 3$, 6 and 9.

$$P(q_i) = \frac{1}{nB} \sum_{k=1}^{n} K\left(\frac{q_i - q_{i,k}}{B}\right) \tag{4}$$

where

$$K\left(\frac{q_i - q_{i,k}}{B}\right) = \frac{1}{\sqrt{2\pi}} e^{-\frac{1}{2}\left(\frac{q_i - q_{i,k}}{B}\right)^2} \tag{5}$$

is the Gaussian non-negative, symmetric weighting function (kernel), B is the smoothing parameter that scales the influence of each observation and control the bias-variance trade-off (low values captures local fluctuations, while large values yields a smoother, more generalized distribution), and $1/\ nB$ is the normalization factor ensuring that $P(q_i)$ integrates to 1 in the domain $[-\infty; \infty]$.

By comparing the estimated densities $P\left(q_i|p_j\right)$, with $i = 1, 2$ and $j = 1, 2, 3, 4$ it is possible to systematically address the role of the investigated parameter on the fragility curves parameters θ and β for the generic DS. Fig. 5 shows the sensitivity of the response variable θ to the input parameters $\boldsymbol{p}$. In detail, each row of graph refers to a specific DS, while in columns the probability density functions conditioned to the different parameters are shown. Similarly, Fig. 6 shows the sensitivity of β to the input parameters $\boldsymbol{p}$. From an overall point of view, the larger the overlap between the distributions conditioned on a parameter p_j, the lower the sensitivity of the parameters θ and β to the specific parameter. In addition, it is worth remembering that θ represents the value of the IM at which there is a 50% probability of exceeding the defined DS, while β quantifies the total uncertainty associated with the damage prediction.

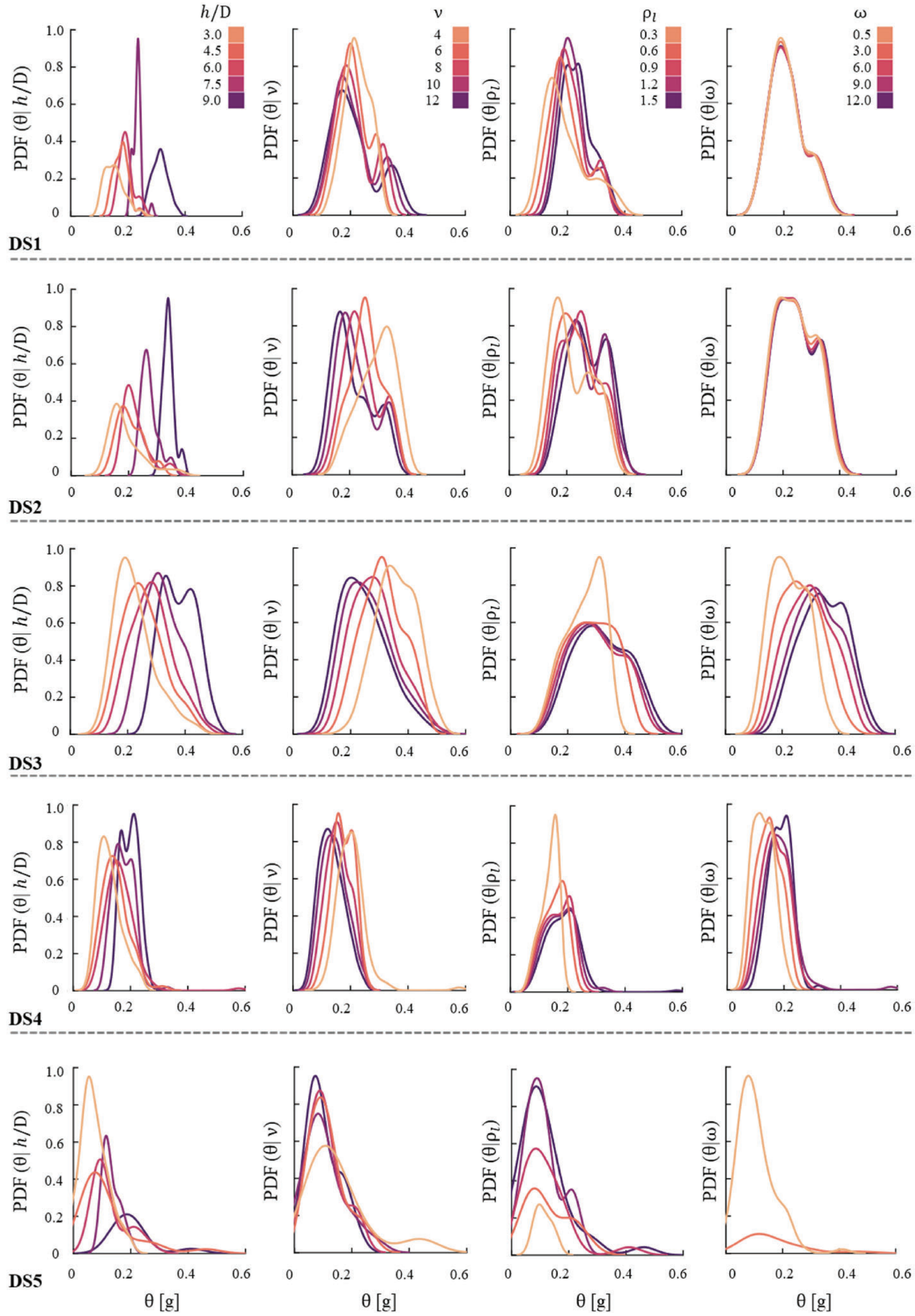

Fig. 5. Conditioned PDF of θ (KDE estimate).

4.1.1. Effect of the slenderness ratio (h/D)

The *h*/D ratio has a primary role on θ for all DSs. As for DS1, by increasing the *h*/D ratio a shift of the conditional PDFs to higher modal values is observed, as well as a change in the distributions shape. The appearance of sharp, isolated peaks for high values of the ratio suggests that these trigger highly localized, high-magnitude response modes, demonstrating that the θ value "locks" into a very specific, repeatable, and narrow range of values. For DS2, DS3 and DS4, a clearer role of the parameter is evident, producing a shift of the conditional PDFs to higher values as *h*/D increases. Furthermore, PDFs are overall narrow and well-separated, with a monotonic trend of the modes, suggesting a deterministic relationship between θ and *h*/D. In addition, high values of *h*/D also trigger the arising of bimodal PDFs, probably due to effects of different set of the remaining parameters in determining the achievement of the DS. Finally, the effect of *h*/D on DS5 is quite complex: indeed, as the ratio increases, the distribution not only shift towards higher values of θ, but also collapses in magnitude and expands in variance. This indicates that for short piers the response is stable and highly predictable, probably because the shear failure is governed by the aspect ratio, while for high piers, uncertainties in the failure mechanisms arise, probably triggered by combination of other set of parameters.

Concerning β, clear trends with the slenderness ratio are only evident for DS3 and DS4, for which, by increasing the *h*/D ratio, a shift of β to higher values is observed, as well as a widening of the PDFs and a reduction of peaks. This suggests that the effect of the parameter on β becomes less predictable as *h*/D increases, as also demonstrated by the tendency of PDFs to show bimodality for high values of the slenderness parameter. The role of the slenderness ratio on the dispersion parameter β for DS1, DS2 and DS5 is less clear, even if a certain overlap of the PDFs

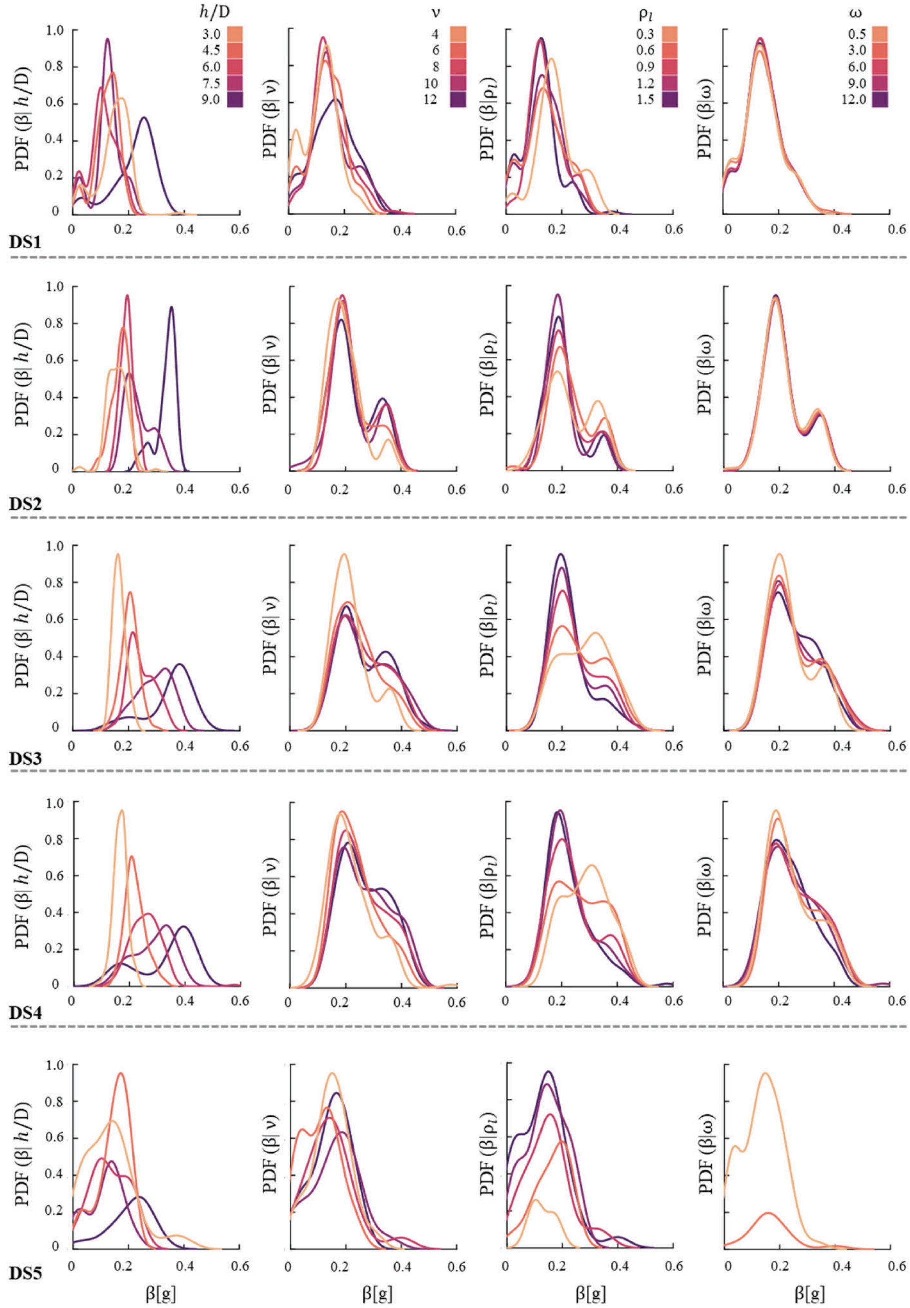

Fig. 6. Conditioned PDF of β (KDE estimate).

can be observed demonstrating the low sensitivity of β to *h*/D, excluding the evident significant shift of the mean value of β observed for DS1 and DS2 in case of tall piers ($h/D = 9$).

4.1.2. *Effect of normalized axial force* (*ν*)

The normalized axial force mainly acts as a scaling factor for parameter θ: across DS1 through DS4, the increase of *ν* induces a shift of PDFs to lower values. This effect is more pronounced for DS2, DS3 rather than for DS1 and DS4. In addition, high values of the ratio are also responsible for bimodal distributions of θ, especially for DS1 and DS2, arising as a contribution of the remining set of parameters. Apart from minor effects (consistent with the arising of bimodal distributions), the peak amplitudes are quite constant, as well as the PDFs width, demonstrating that the parameter variation probably does not significantly alter the failure mechanisms. As for DS5, by increasing *ν*, θ slightly moves toward lower values while simultaneously becoming narrower and taller; this indicates that as *ν* increases, its effect on θ becomes more predictable, with a significant reduction of uncertainty for high *ν* values.

The sensitivity of β to the normalized axial force seems to be low for all the DSs, as demonstrated by the almost superimposed PDFs relative to different *ν* values.

4.1.3. *Effect of longitudinal reinforcement* (ρ_l)

As for DS1, by increasing the longitudinal reinforcement, a minor shift of the PDFs to higher values of θ is observed, while overall preserving the sharpness of peaks; this suggests that for DS1, the longitudinal reinforcements scale the IM corresponding to the 50% probability of exceeding the DS, without introducing uncertainties in the failure modalities. This appears reasonable in view of the damage type (first yielding of the cross-section). For DS2, the sensitivity of θ to the longitudinal reinforcement reveals instead the emergence of a secondary mode, indicating that the parameter presents a competitive interaction with the remaining ones to determine the achievement of the DS. For DS3 and DS4 instead, a less pronounced sensitivity of the response to the longitudinal reinforcement is observed, consistently with the damage mechanisms that, beyond the elastic field, are mainly related to the displacement demand. For DS5, a reduction of the reinforcement led to a reduction of the PDFs width and amplitude, while preserving the mean value of θ; this implies that lower parameter values correlate with a loss of predictive confidence.

Like for the previous parameter, the sensitivity of β to the longitudinal reinforcement ratio seems to be low for all the DSs, as demonstrated by the almost superimposed PDFs relative to different ρ_l values. However, for DS2, DS3 and DS4, low values of ρ_l lead to bimodal distributions for β, revealing a significant interaction with the remaining parameters. Overall, by increasing ρ_l, the β values for the above DSs became more predictable and less uncertain, as well as less sensitive to ρ_l. For DS5, a reduction of the reinforcement led to a reduction of the PDFs width and amplitude, while preserving the mean value of β; this implies that lower parameter values correlate with a loss of predictive confidence.

4.1.4. Effect of transverse reinforcement volumetric ratio (ω)

As expected, the transverse reinforcement volumetric ratio has no influence of the mean values and confidence of θ, because of the damage typologies, which are mainly related to the longitudinal reinforcement. As for DS3, the amount of transverse reinforcement positively affects the pier ductility producing a shift of the θ mean value towards higher values, although a slight increase of the PDFs width demonstrates an increase of the estimation uncertainty. Finally, the parameter has a great effect on DS5; however, the absence of curves is related to the absence of DS5 failure type for high values of ω.

The sensitivity of β to the transverse reinforcement volumetric ratio ω is not significant for all the DSs.

4.2. Prediction tools for the seismic fragility of circular piers

Fragility curves represent a key tool for assessing the reliability and resilience of transportation networks in seismic areas, as well as an effective support for decision-making processes. However, their derivation generally requires complex and computationally demanding analyses. Consequently, in recent years there has been growing interest in the development and use of alternative, more efficient, and simplified models for estimating fragility curves. In the field of buildings, several approaches have been proposed in the literature, including the use of Machine Learning procedures, e.g. [41]. Innovative techniques have also been widely applied in the field of bridge engineering. Mangalathu and Jeon [42] propose an approach for classifying failure modes using machine-learning algorithms. Stefanidou et al. [43] present an online platform for deriving fragility curves of bridge piers and for computing limit-state thresholds, based on closed-form relationships for different pier typologies, both as-built and retrofitted. Finally, Wang et al. [44] employ genetic programming to generate equations capable of estimating the statistical parameters of fragility curves for both the damage and the ultimate limit states.

Within this context, the present work proposes multiparametric regression models and an Artificial Neural Network (ANN) based on the large dataset of the performed applications for defining parameters of fragility curves for circular reinforced concrete bridge piers. In detail, the former favors the reduced computational effort and assures a direct control on the complexity of the resulting regression formulas avoiding overfitting issues, while the latter exploits advantages of routines based on artificial intelligence for identifying complex pattern within the dataset. Both methods allow the prediction of fragility curves parameters for all the considered DSs.

4.2.1. Multivariate regression analysis

For the prediction of parameters θ and β, i.e. the median and standard deviation of the cumulative probability density functions constituting the fragility curves associated to the different DSs, a multivariate iterative regression approach was adopted.

In order to get a formula of general validity and adequately represent potential nonlinearities and interdependencies among the independent variables (h/D, ν, ρ_l, ω), the regression model was extended to include second-order polynomial combinations, as well as exponential, logarithmic, and hyperbolic functional forms. The contribution of each term to the regression equation was systematically evaluated on the basis of its statistical significance and the overall goodness of fit, as quantified by the coefficient of determination (R^2).

The analysis was initially conducted using a linear model relating the target parameter to the independent variables, with particular attention to both the quality of fit and the statistical relevance of the predictors. Subsequently, nonlinear terms were introduced in a stepwise manner. At each stage, only those terms satisfying the prescribed statistical significance criterion were retained in the model.

Specifically, the statistical significance of the regression coefficients was assessed using p-values. Under the null hypothesis that a given coefficient is equal to zero (i.e., the corresponding variable has no effect on the dependent parameter), the p-value represents the probability of observing a coefficient at least as extreme as the estimated one. A significance level of 5% was adopted; thus, terms with p-values below 0.05 were considered statistically significant and retained in the model, while those exceeding this threshold were excluded.

The general form of the resulting model is as follows:

$$\begin{aligned}\widetilde{q}_i(\mathbf{p}) = {} & a_0 + a_1p_1 + a_2p_2 + a_3p_3 + a_4p_4 + a_5p_1^2 + a_6p_2^2 + a_7p_3^2 + a_8p_4^2 \\ & + a_9\, ln(p_1) + a_{10}\, ln(p_3) + a_{11}e^{p_1} + a_{12}e^{p_2} + a_{13}e^{p_4} + a_{14}p_1p_2 \\ & + a_{15}p_1p_3 + a_{16}p_1p_4 + a_{17}p_2p_3 + a_{18}p_2p_4 + a_{19}p_3p_4\end{aligned} \tag{6}$$

where $\widetilde{q}_i$ is the predicted i-th parameter $(\widetilde{\theta}, \widetilde{\beta})$ relevant to the generic DS, and $\boldsymbol{p} = [\,h/D \quad \nu \quad \rho_l \quad \omega\,]$ is the vector of the independent variables.

Table 3 reports, for each parameter of interest, coefficients of equation (6), together with the adjusted coefficient of determination R^2, which overall quantifies the goodness of fit of the regression model.

In order to provide an overview of the goodness of fit, Figs. 7a and 8a compare, in logarithmic scale, the data obtained from the analyses and the corresponding values predicted by the multivariate regression model, for each parameter (θ and β) and for each DS. Plots allow capturing the fit quality by observing the points distribution with respect to the plot diagonal (identity line). To support this visual assessment, each comparison also reports the adjusted R^2 value and includes an error band around the identity line, corresponding to ±15% the analysis data.

Besides the previous comparison, Figs. 7b and 8b show the percentage relative error ε obtained from:

$$\varepsilon_{i,j} = \frac{\widetilde{q}_i\left(\mathbf{p}_j\right) - q_i\left(\mathbf{p}_j\right)}{q_i\left(\mathbf{p}_j\right)} \quad (j = 1\ldots625) \tag{7}$$

where subscript i refers to the i-th parameter of the DS at hand, while j provides the variability of the case studies. In addition, $\widetilde{q}_i\left(\mathbf{p}_j\right)$ is the predicted i-th fragility curve parameter for the j-th set of independent parameters, and $q_i\left(\mathbf{p}_j\right)$ is the corresponding value obtained from the numerical applications. Residual plots offer an additional tool for evaluating the adequacy of the regression calibration revealing any potential bias or systematic error (i.e. if residuals appear randomly scattered around zero without identifiable patterns, no unmodelled relationships nor residual dependencies are present). When these conditions are met, the model can be considered well calibrated and the explanatory variables adequate for describing the phenomenon without neglecting

Table 3
Coefficients for the definition of the multivariate regression model.

Parameter	$\widetilde{\theta}_{DS1}\|IM$	$\widetilde{\beta}_{DS1}\|IM$	$\widetilde{\theta}_{DS2}\|IM$	$\widetilde{\beta}_{DS2}\|IM$	$\widetilde{\theta}_{DS3}\|IM$	$\widetilde{\beta}_{DS3}\|IM$	$\widetilde{\theta}_{DS4}\|IM$	$\widetilde{\beta}_{DS4}\|IM$	$\widetilde{\theta}_{DS5}\|IM$	$\widetilde{\beta}_{DS5}\|IM$
a_0	0.1508	-	0.5302	0.2536	0.7194	-	0.8721	0.1841	-	-
a_1	−0.2616	−0.3811	−0.0619	−0.0473	-	0.0333	-	0.0269	-	−0.5901
a_2	−0.0195	-	−0.0474	-	−0.0917	0.0085	−0.1243	−0.0220	-	-
a_3	0.1362	0.3432	0.4078	-	0.1888	-	0.2769	-	-	3.9284
a_4	-	-	-	-	0.0311	0.0126	0.0467	-	-	−1.0597
a_5	0.0140	0.0209	0.0083	0.0062	0.0022	-	-	-	-	-
a_6	0.0005	-	0.0016	−0.0005	0.0028	−0.0014	0.0040	-	-	-
a_7	-	−0.0820	-	-	-	-	-	-	-	-
a_8	-	-	-	-	−0.0012	−0.0005	−0.0019	-	-	-
a_9	0.6037	0.7654	-	-	-	-	-	-	-	-
a_{10}	-	−0.1343	-	-	-	-	-	-	-	-
a_{11}	-	-	-	-	-	-	-	-	-	-
a_{12}	-	−1.6E-07	-	-	-	-	-	-	-	-
a_{13}	-	-	-	-	-	-	-	-	-	1.2E-05
a_{14}	0.0024	0.0014	0.0038	0.0012	0.0046	0.0023	0.0070	0.0029	-	-
a_{15}	−0.0103	−0.0098	−0.0222	−0.0100	-	−0.0172	0.0101	−0.0191	-	-
a_{16}	-	-	-	-	-	−0.0009	−0.0014	−0.0012	0.1175	-
a_{17}	−0.0050	-	−0.0230	0.0044	−0.0164	0.0074	−0.0275	0.0074	-	-
a_{18}	-	-	-	-	-	-	-	0.0007	−0.0074	-
a_{19}	-	-	-	-	0.0108	-	0.0140	-	−0.1730	-
R^2	0.9722	0.9030	0.9588	0.8228	0.9463	0.9750	0.8682	0.6544	0.9028	0.2053

significant components. In this study, relative errors are shown emphasising the percentage deviation between the regression estimates and the actual data. Although the relative error provides information similar to that of residuals, it may exhibit greater variability, with larger deviations occurring for lower-valued observations. For this reason, each plot also reports the Root Mean Square error (RMS), which quantifies the dispersion of the errors in the same unit of the variable and provides a measure of the predictive performance of the model.

$$\varepsilon_i^{RMS} = \sqrt{\frac{1}{J}\sum_{j=1}^{J}\left(\widetilde{q}_i\left(\mathbf{p}_j\right) - q_i\left(\mathbf{p}_j\right)\right)^2}\ (J = 625) \tag{8}$$

As shown for all regressions of θ in Fig. 7a, points align well with the diagonal, indicating a strong model agreement, even if some outliers are evident for DS5. Above consideration is supported by adjusted R^2 values, which are overall very high, ranging from 0.87 (for DS4) to 0.97 (for DS1). The residual plots show no discernible patterns, with points scattered around zero, and the relative error remains mostly within the ±15% band, except for the parameter corresponding to the shear damage state (DS5). In this case, both the dispersion and the RMSE increase, which may be attributed to the smaller amount of data available for DS5 compared with the other damage states. Indeed, a reduced sample size typically leads to less stable parameter estimates and consequently to lower model performance and less favourable statistical indicators.

Concerning β, a less accurate regression is highlighted by graphs of Fig. 8. For all the DSs, points are more widely scattered around the diagonal, indicating an average error generally exceeding 15%. The largest deviations are observed for DS1 and especially for DS5, where the regression model exhibits its greatest shortcomings. The relative errors and the root mean square error shown in Fig. 8b confirm the aforementioned conclusions.

In order to improve the estimation of the fragility curve parameters, especially for what concern the β parameter, an approach involving the use of the artificial intelligence was adopted, developing an Artificial Neural Network (ANN).

4.2.2. *Artificial Neural Network*

With the aim of improving the prediction of fragility curves, an artificial neural network (ANN) was developed, given its capability to identify complex patterns and relationships even in unstructured datasets. ANNs consist of highly interconnected nodes, or "neurons," organized in layers that process information by responding to external inputs and transmitting signals between units. This process enables the network to learn relationships within the data and to make predictions for new, unseen inputs.

The neural network employed in this study is a feed-forward network, characterized by a unidirectional flow of information from the input layer to the output layer. For the *i*-th DS fragility, the ANN architecture includes an input layer composed of 4 nodes relevant to the parameters **p**, and an output layer of 1 neuron, corresponding to the generic distribution parameter (θ and β) of the *i*-th DS. No hyperparameters are considered; inputs are transmitted to a sequence of hidden layers, which constitute the true computational core of the network. In these layers, each neuron combines the received inputs with their associated weights and processes them through an activation function. The weights are initialized and subsequently optimized during the training phase through a backpropagation process aimed at minimizing the loss function. The larger the weight associated with a given input, the greater its influence on the neuron's output. The output generated by each neuron in one layer becomes the input for the next, propagating information throughout the network until it reaches the output layer, which returns the predicted value of the target parameter.

For this work, a network with 100 hidden layers was implemented, a choice motivated by the complexity of the phenomenon under investigation and its pronounced nonlinearity, already highlighted by the nonlinear multiparametric regression model. The hyperbolic tangent (tanh) activation function was adopted, as it is particularly suitable for models involving nonlinear relationships. Network training was performed using the Limited memory Broyden-Fletcher-Goldfarb-Shanno (LBFGS) optimization algorithm [45], adopting a tolerance of 1E-6, a maximum of 20000 iterations and a constant learning rate.

To assess the performance of the ANN, graphical comparisons between the predicted and actual values of θ and β are shown in Fig. 9 and Fig. 10 for parameters θ and β, respectively, following the same approach used for the nonlinear multiparametric regression. Results indicate that the neural network provides a satisfactory estimation of all analyzed parameters: plots in Figs. 9a and 10a show good alignment between observed and predicted data, while the residuals in Figs. 9b and 10b appear randomly scattered around zero, suggesting the absence of bias or unmodeled relationships. Overall, the neural network proves to be an effective tool for capturing complex relationships and inferences that are difficult to identify using traditional statistical models, even when enhanced with nonlinear terms. The most significant improvement with respect to the nonlinear multiparametric regression approach is observed in the estimation of the parameters associated with DS5, where a substantial reduction in the root-mean-square error (RMSE) is

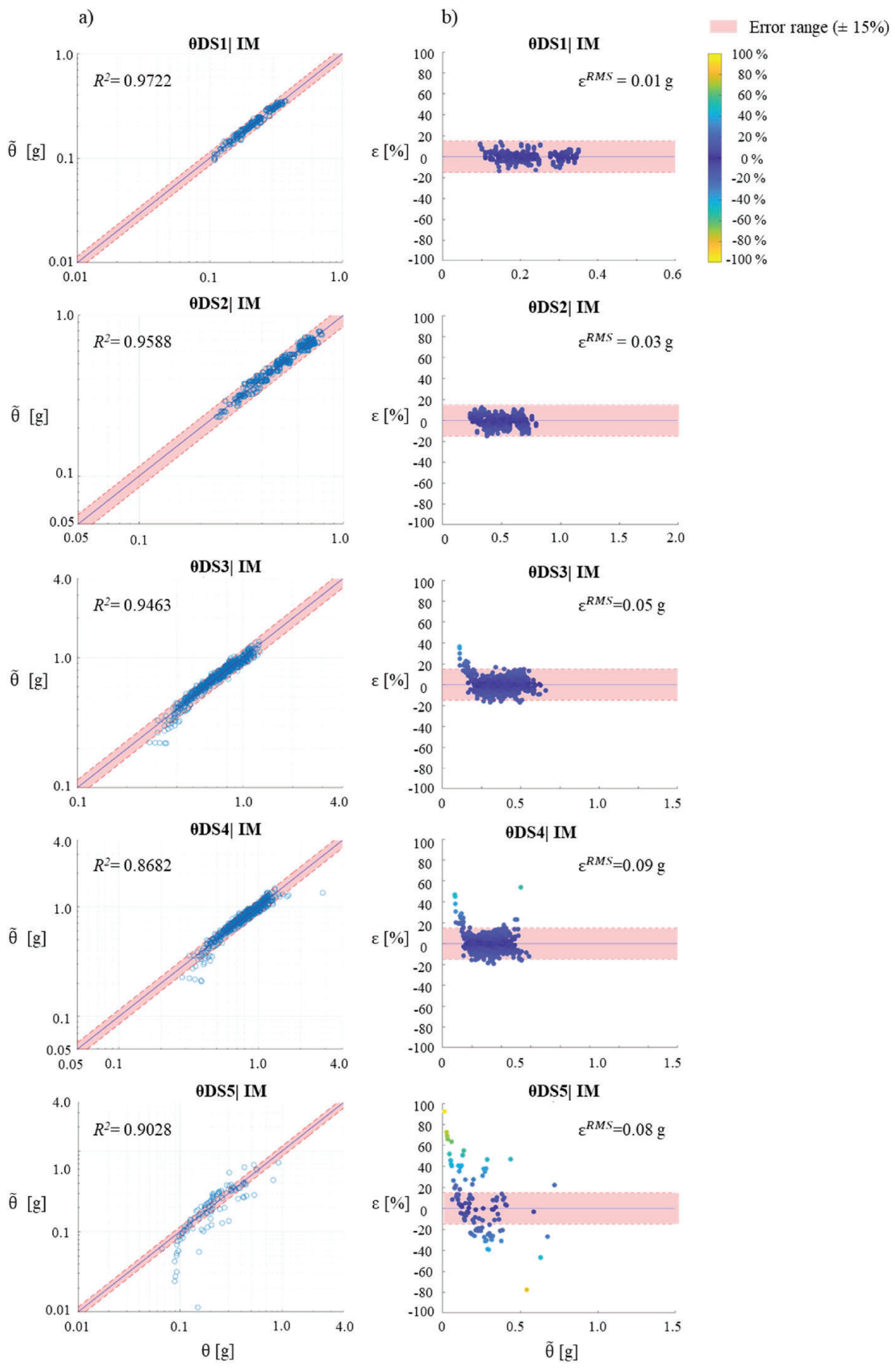

Fig. 7. a) Correlation between actual and predicted values of θ (multivariate regression), b) Residual plots.

achieved, indicating a marked enhancement in predictive capability compared to the regression model.

5. Application of the proposed fragility tools for constructing damage map

The purpose of this section is to demonstrate direct applications of the developed tools, highlighting their relevance and applicability in the framework of the post-earthquake emergency management. Tools presented in the previous section for fragility curves prediction are herein used to develop exceedance probability damage maps for a specific DS of the selected bridge taxonomy, conditioned to observed ground-motion fields resulting from classical shake maps generated after the occurrence of seismic events. Furthermore, tools can be integrated into bridge structural monitoring systems equipped with free-field motion sensors providing real-time post-earthquake information on structural health in terms of conditional exceedance probability for a specific DS which can be visualized and managed through GIS-based mapping platforms to support rapid decision-making and emergency response activities.

Referring to damage maps, these can be obtained by combining fragility information with the shake maps, providing indications on the probability of exceedance of a damage state for specific class of bridges over the territory struck by an earthquake. It is worth noting that such maps are not intended to explicitly represent seismic risk [46], and

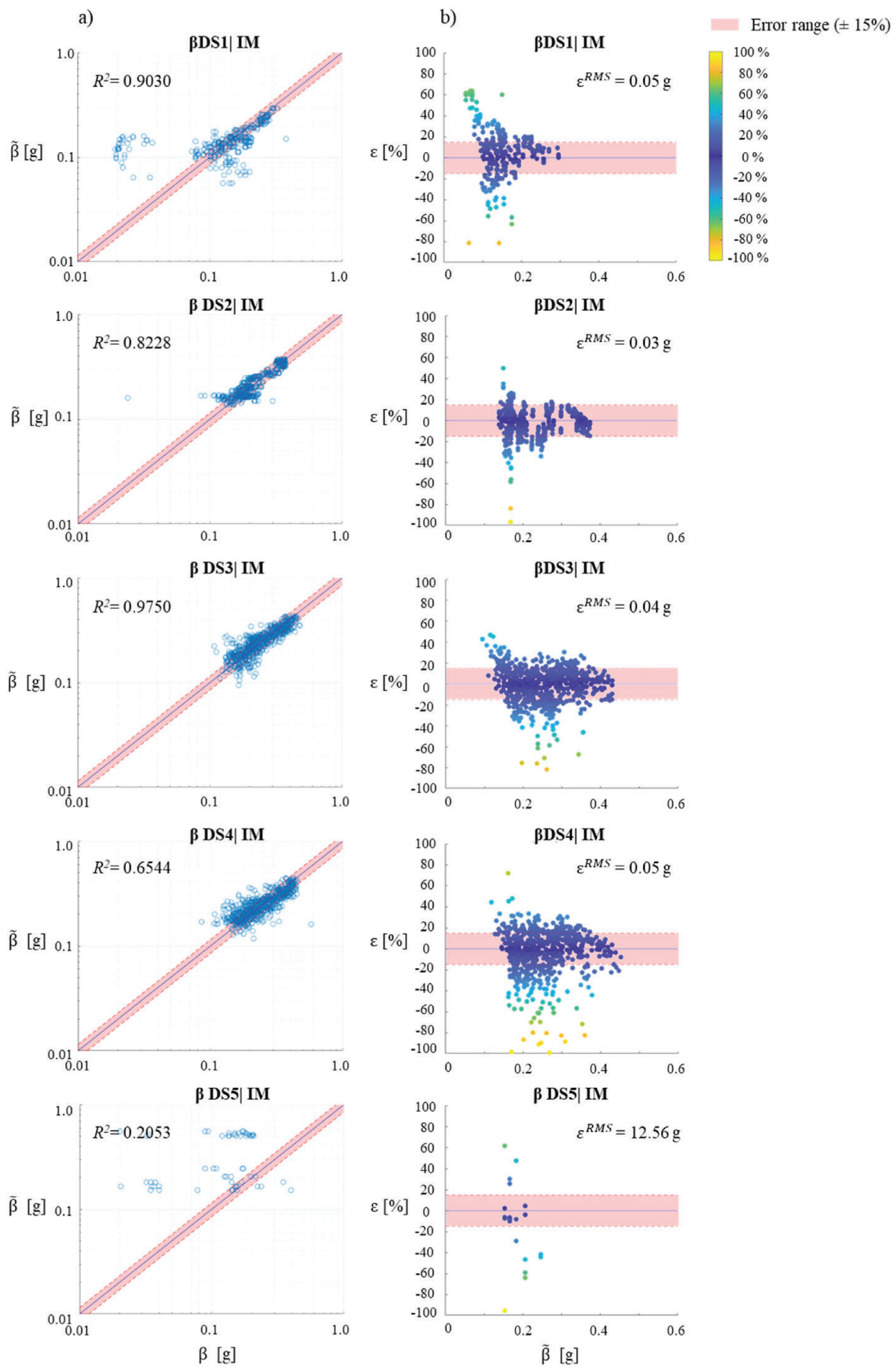

Fig. 8. a) Correlation between actual and predicted values of β (multivariate regression), b) Residual plots.

should not be interpreted as predictive tools. Rather, they are conditioned on observed IM fields and are therefore unaffected by the uncertainties associated with ground-motion prediction. As such, they can play a crucial role in post-earthquake emergency management by supporting the prioritization of structural inspections and safety assessments. In addition, they can facilitate the identification of safe transportation routes for rescue and recovery operations, thereby contributing to a more efficient allocation of resources and a more effective emergency response.

In this study, the maps were produced using data from the shake maps providing grids of geographic points with associated PGAs values. For each point in the grid, the PGA value was used as the input parameter for the fragility curves. Given a specific DS (to which a specific d_i is associated), damage maps can be constructed for bridge classes, where the classification can be based on the generic parameter $p_i \in \mathbf{p}$. To account for the effects of the remaining parameters variability on the bridge class fragility, the conditional PDF $f_{P,c}\left(P_{d\geq d_i}\middle|p_i, IM\right)$ is numerically computed (subscript c refers to the c-th class of bridges determined by the selection of parameter p_i). Consequently, the variability of the damage probability within the class is addressed in a statistical manner by selecting a desired percentile α for the damage probability

$$P_{c,\alpha}\middle|IM = F_{P,c}^{-1}(\alpha) \tag{9}$$

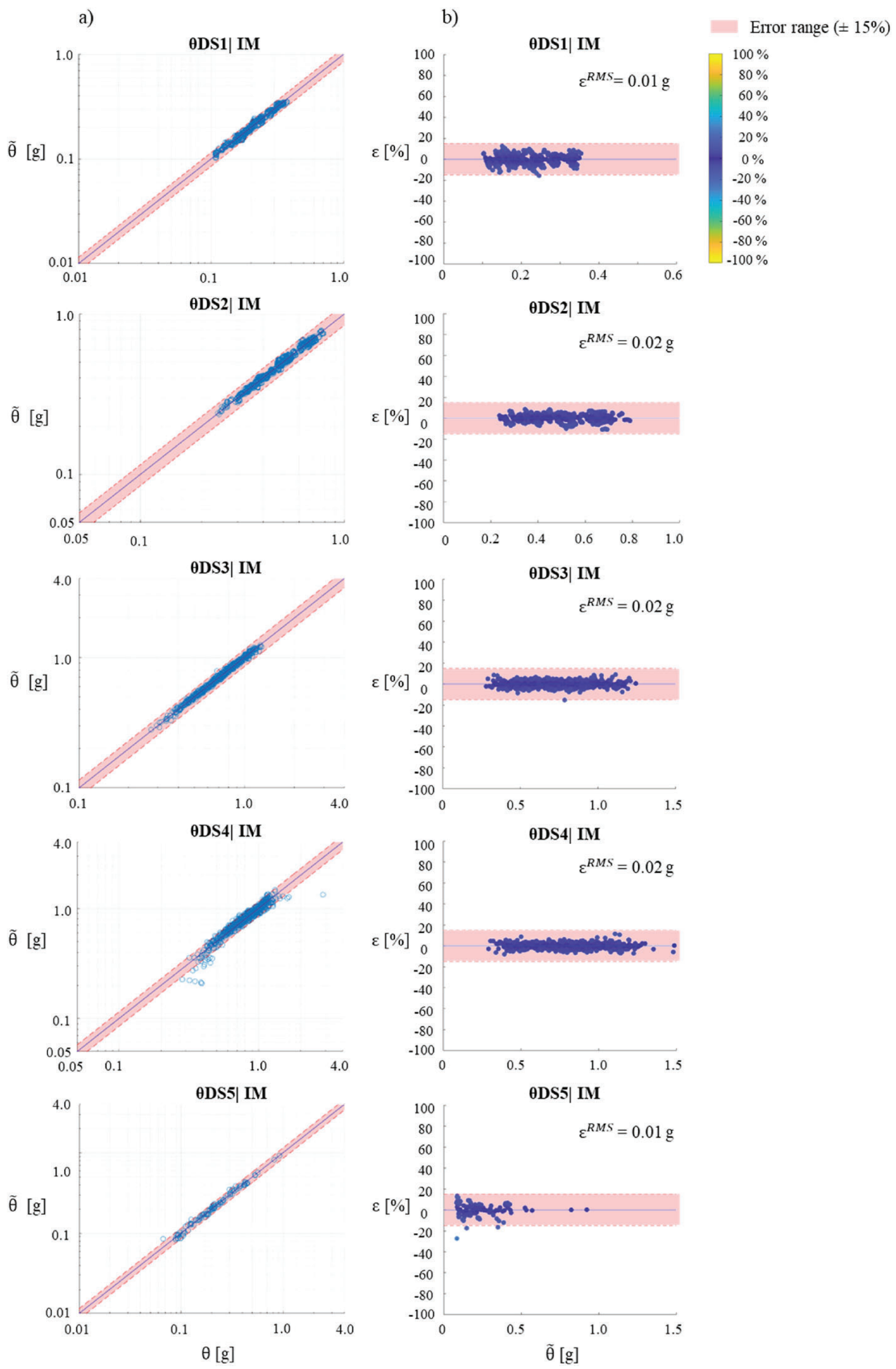

Fig. 9. a) Correlation between actual and predicted values of θ (ANN), b) Residual plots.

where $F_{P,c}$ is the CDF of $f_{P,c}$.

In practice, damage maps associated with specific bridge classes characterized by different slenderness ratios are considered. To provide a graphical overview of the procedure, Fig. 11 shows for the bridge class identified by $h/D = 9$, the fragility curves obtained by considering the overall variability of the investigated parameters as well as the PDF $f_{P,c}$, conditioned to IM = 1 g and IM = 1.2 g. In the same figure, the percentiles adopted in the sequel (84th, 50th and 16th) are also graphically reported.

Once the exceedance probability is obtained for each point in the grid, the data can be interpolated to identify areas of the geographic map characterized by specific exceedance-probability intervals (iso-damage lines can also be obtained if necessary). In Fig. 12, an application of the method described above is shown for a real case. The application was developed using the shake map provided by Italian National Institute of Geophysics and Vulcanology for the 30th October 2016 seismic event of Mw 6.5, with epicenter near Norcia, in Central Italy. Maps are produced for the three above mentioned percentiles (16, 50, and 84) and for three values of the slenderness ratio (3, 6, and 9) focusing on the performance level associated to DS3. Within each map, the probability of exceedance of the damage state is represented using a color-gradient mesh, while PGA values are illustrated through contour lines, also associated with a corresponding color gradient.

From the map observation, it can be observed that the highest

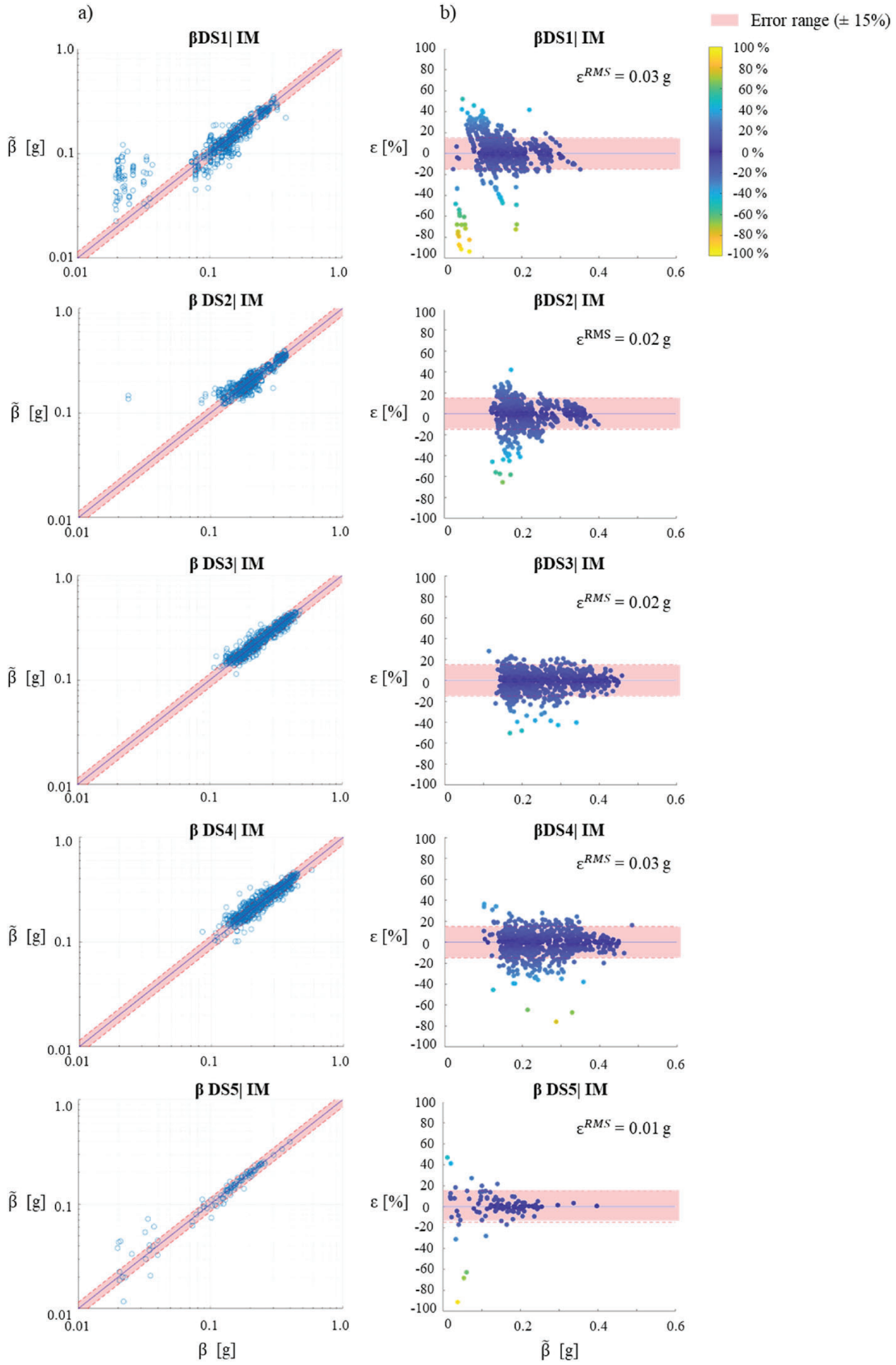

Fig. 10. a) Correlation between actual and predicted values of β (ANN), b) Residual plots.

damage probabilities are concentrated in the epicentral area of the seismic event, where the largest PGA values were recorded. In particular, the highest probability of exceedance damage DS3 occurs for short piers (h/D = 3), for which values between 90% and 100% are reached for the 84th percentile, with residual values up to 40% for the 16th percentile. The higher tendency to reach DS3 when the h/D ratio is equal to 3 is associated with the higher acceleration to which the pier is subjected; in fact, a pier characterized by a larger h/D ratio exhibits higher natural vibration periods, which generally correspond to lower seismic accelerations.

6. Conclusions

A robust computational framework for the seismic assessment of circular reinforced concrete bridge piers has been presented in this work, moving beyond individual case studies. The parametric study included a wide range of pier configurations, varying the height-to-diameter ratio, the normalized axial load, the longitudinal reinforcement ratio, and the transverse reinforcement volumetric ratio. Nonlinear time-history analyses were performed using multiple stripe analysis to derive fragility curves for five distinct damage states, ranging from initial yielding to collapse, including both ductile and brittle failure mechanisms. The role of the parameters on the seismic response is

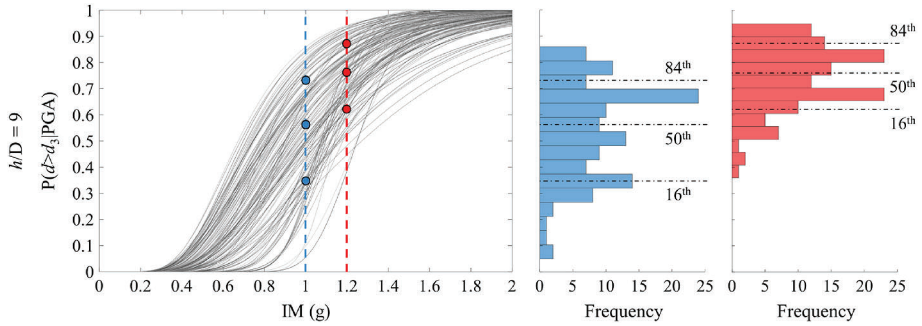

Fig. 11. Distribution of the damage probabilities for the pier class $h/\mathrm{D} = 9$.

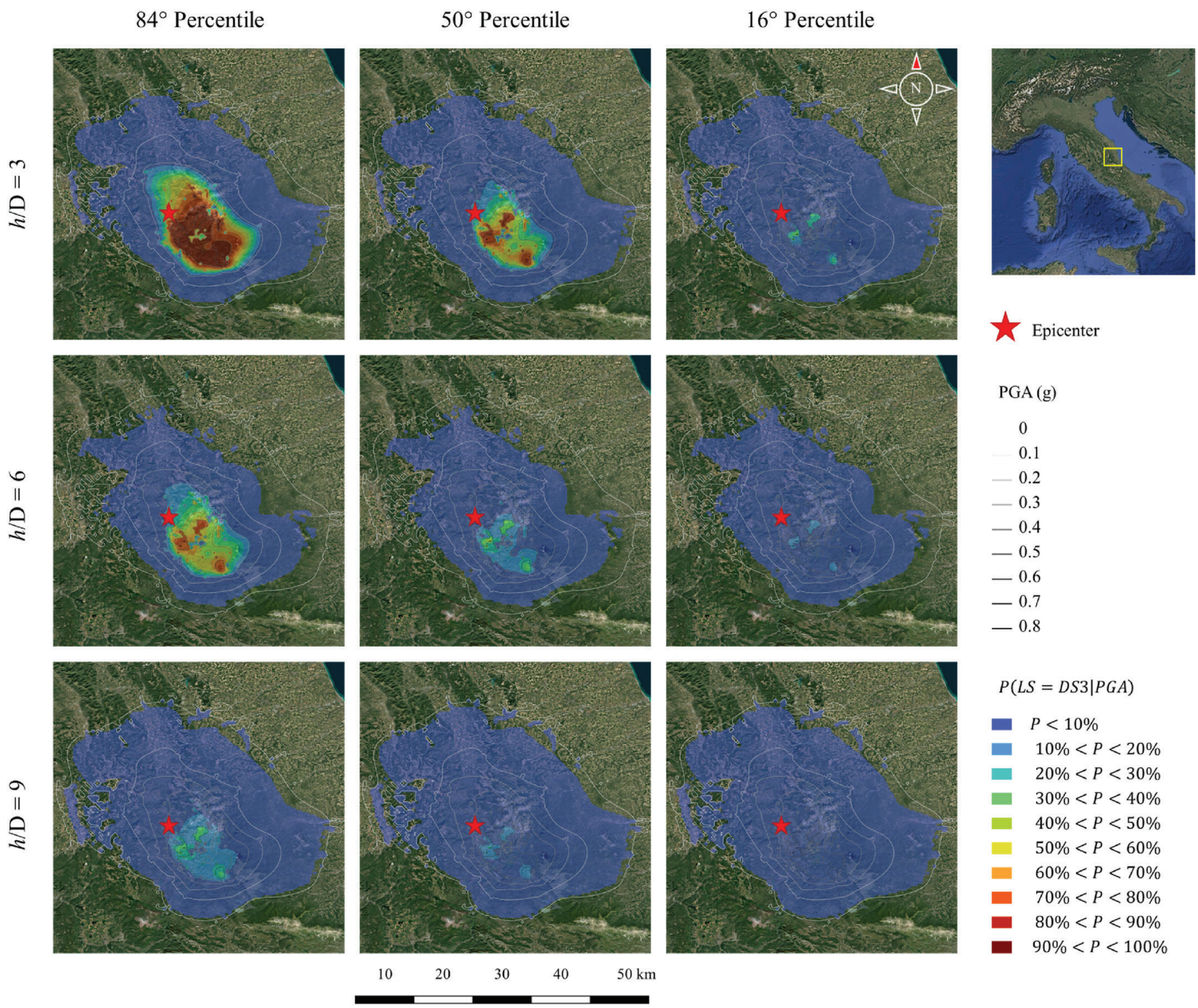

Fig. 12. Probability maps of the DS3 at 16th, 50th and 84th percentile, for pier classes $h/\mathrm{D} = 3$, 6 and 9.

studied by systematically addressing the sensitivity of fragility parameters to the investigated input variables.

Furthermore, generalized predictive tools for estimating the fragility of the specific bridge taxonomy are provided, overpassing the need of computationally expensive nonlinear analyses. The latter includes multivariate regression models and artificial neural network algorithms that proven to be highly accurate in predicting the pier fragility. Finally, the applicability of these tools is demonstrated through the generation of damage maps for post-earthquake decision-making and emergency management.

Besides a contribution on the understanding of the fragility sensitivity to geometric and mechanical properties of bridges, the developed tools enable the rapid evaluation of large stocks of existing bridges by requiring only basic geometric and mechanical data as input. By providing a direct correlation between structural and fragility parameters, these models serve as a fundamental component for seismic risk management platforms and prioritization strategies for retrofitting interventions as well as for defining IM-based alert thresholds to be used in the field of structural health monitoring systems. Furthermore, the integration of these fragility models into damage mapping procedures allows for near real-time post-earthquake scenarios; as demonstrated in the case study, maps are essential for identifying the most vulnerable criticalities in the transportation network and optimizing rescue and recovery logistics.

In conclusion, the research provides bridge owners and civil protection agencies with a ready-to-use toolkit for enhancing infrastructure resilience, offering a scientifically grounded basis for both long-term planning and emergency response.

CRediT authorship contribution statement

R. Martini: Data curation, Formal analysis, Methodology, Software, Visualization, Writing – original draft. **L. Tentella:** Data curation, Formal analysis, Methodology, Software, Visualization, Writing – original draft. **A. Brunetti:** Data curation, Formal analysis, Software, Visualization, Writing – original draft. **S. Carbonari:** Conceptualization, Methodology, Supervision, Validation, Writing – review & editing. **F. Gara:** Conceptualization, Methodology, Supervision, Writing – review & editing.

Declaration of competing interest

The authors declare that they have no known competing financial interests or personal relationships that could have appeared to influence the work reported in this paper.

Data availability

Data will be made available on request.

References

[1] Kawashima K. Seismic performance of RC bridge piers in Japan: an evaluation after the 1995 Hyogo-ken nanbu earthquake. Prog Struct Eng Mater 2000;2:82–91. https://doi.org/10.1002/(SICI)1528-2716(200001/03)2:1%3C82::AID-PSE10%3E3.0.CO;2-C.

[2] Priestley MJN, Seible F, Calvi GM. Seismic design and retrofit of bridges. New York, New York, USA: Jhon Wiley & Sons, Inc.; 1996.

[3] Cornell CA, Jalayer F, Hamburger RO, Foutch DA. Probabilistic basis for 2000 SAC federal emergency Management Agency Steel Moment Frame Guidelines. J Struct Eng 2002;128:526–33. https://doi.org/10.1061/(ASCE)0733-9445(2002)128:4(526.

[4] Porter KA. An overview of PEER's performance-based earthquake engineering methodology. In: Proc. 9th int. Conf. Appl. Stat. Probab. Civ. Eng. ICASP9; 2003.

[5] Federal Emergency Management Agency (FEMA). Seismic performance assessment of buildings. 2012.

[6] Baraschino R, Baltzopoulos G, Iervolino I. R2R-EU: software for fragility fitting and evaluation of estimation uncertainty in seismic risk analysis. Soil Dynam Earthq Eng 2020;132:106093. https://doi.org/10.1016/j.soildyn.2020.106093.

[7] Nettis A, Gentile R, Raffaele D, Uva G, Galasso C. Cloud Capacity Spectrum Method: accounting for record-to-record variability in fragility analysis using nonlinear static procedures. Soil Dynam Earthq Eng 2021;150:106829. https://doi.org/10.1016/j.soildyn.2021.106829.

[8] Nielson BG, DesRoches R. Analytical seismic fragility curves for typical bridges in the central and Southeastern United States. Earthq Spectra 2007;23:615–33. https://doi.org/10.1193/1.2756815.

[9] Shinozuka M, Feng MQ, Lee J, Naganuma T. Statistical analysis of fragility curves. Multidisciplinary Center for Earthquake Engineering Research 2003. https://doi.org/10.1061/(ASCE)0733-9399(2000)126:12(1224. Los Angeles, California.

[10] Ruggieri S, Nettis A, Raffaele D, Guido B, Uva G. Seismic fragility and risk assessment of Reinforced Concrete bridges undergoing elastomeric bearing deformations induced by landslide. Int J Bridge Eng Manag Res 2024;1. https://doi.org/10.70465/ber.v1i1.6. 21424003–1:13.

[11] Tubaldi E, Dall'Asta A, Dezi L. Reduced formulation for post-elastic seismic response of dual load path bridges. Eng Struct 2013;51:178–87. https://doi.org/10.1016/j.engstruct.2013.01.014.

[12] Mander JB, Priestley MJN, Park R. Theoretical stress-strain model for confined concrete. J Struct Eng 1988;114:1804–26. https://doi.org/10.1061/(ASCE)0733-9445(1988)114:8(1804.

[13] Priestley MJN, Calvi GM, Kowalsky MJ. Displacement-Based seismic design of structures. Pavia, Italy: IUSS Press; 2007. https://bookstore.eucentre.it/prodotto/displacement-based-seismic-design-of-structures-2nd-edition/. [Accessed 6 May 2024].

[14] RELUIS. WP4-MARS: mappe di Rischio e Scenari di danno sismico, Task 4.9: Modelli e curve di fragilità dei ponti. DPC-RELUIS; 2019.

[15] RELUIS. The implicit risk of code-conforming structures in Italy. https://www.reluis.it/divulgazione/pubblicazioni/139/the-implicit-risk-of-code-conforming-structures-in-italy-a-joint-reluis-eucentre-project/. [Accessed 7 May 2026].

[16] Borzi B, Ceresa P, Franchin P, Noto F, Calvi GM, Pinto PE. Seismic vulnerability of the Italian roadway Bridge stock. Earthq Spectra 2015;31:2137–61. https://doi.org/10.1193/070413EQS190M.

[17] Miano A, Iacovazzo P, Mele A, Di Ludovico M, Prota A. Seismic fragility of circular piers in simply supported RC bridges: a proposal for capacity assessment. Eng Struct 2024;302:117426. https://doi.org/10.1016/j.engstruct.2023.117426.

[18] Di Mucci VM, Cardellicchio A, Ruggieri S, Nettis A, Renò V, Uva G. Computer vision-based seismic assessment of RC simply supported bridges characterized by corroded circular piers. Bull Earthq Eng 2025;23:6771–800. https://doi.org/10.1007/s10518-025-02291-x.

[19] Nettis A, Di Mucci VM, Cardellicchio A, Ruggieri S, Renò V, Uva G. AI-assisted seismic fragility assessment of corroded RC bridge piers. Procedia Struct Integr 2026;78:1404–11. https://doi.org/10.1016/j.prostr.2025.12.179.

[20] Di Mucci VM, Cardellicchio A, Ruggieri S, Nettis A, Renò V, Uva G. Artificial intelligence in structural health management of existing bridges. Autom ConStruct 2024;167:105719. https://doi.org/10.1016/j.autcon.2024.105719.

[21] Jara JM, Montes O, Olmos BA, Martinez G, Jara JM, Montes O, Olmos BA, Martinez G. Parametric study of medium span bridges retrofitted with reinforced concrete jacketing. Can J Civ Eng 2019;46:567–80.

[22] Olmos B, Jara J, Martinez G. Evaluation of the seismic response of bridges reinforced with reinforced concrete jackets. Proc. REHABEND; 2016, 2016.

[23] CEN. Eurocode 8 - design of structures for earthquake resistance - part 1-1: general rules and seismic action. 2024.

[24] CC.LL.PP. Istruzioni relative alla normativa tecnica dei ponti stradali. 1991.

[25] Salvatore W, Uva G, Venanzi I, Mazzotti C, Morici M, Natali A, Dall'Asta A, Ubertini F, Mannella P, Lepori L, Pellicanò F, Calò M, Cardillo E, Nettis A, Bencivenga P, Brando G, Borlenghi P, Carbonari S, Clemente P, D'amato M, De Matteis G, Di Lallo Y, Facconi L, Gara F, Gattesco N, Gentile C, Ierimonti L, Lomonaco A, Manarin S, Masciotta G, Mazzelli A, Meoni A, Messina V, Minelli F, Noè S, Pellegrino C, Puntel E, Quaglini V, Ragni L, Ranaldo A, Sangiuliano L, Ruggieri S, Zanini M, Zizi M, Zona A, Caliò I, Ferro GA, Fossetti M, Lupoi A, Proverbio E. Application of Italian Guidelines for structural-foundational and seismic risk classification of bridges: the Fabre experience on a large bridge inventory. Procedia Struct Integr 2024;62:1–8. https://doi.org/10.1016/j.prostr.2024.09.009.

[26] McKenna F, Fenves GL, Scott MH. Open System for earthquake engineering simulations. 2000.

[27] Takeda T, Sozen MA, Nielsen NN. Reinforced CONCRETE RESPONSE to simulated earthquake. J Struct Div 1970;96(12):2557–73.

[28] Popovics S. A numerical approach to the complete stress-strain curve of concrete. Cement Concr Res 1973;3:583–99. https://doi.org/10.1016/0008-8846(73)90096-3.

[29] Chang GA, Mander JB. Seismic energy based fatigue damage analysis of bridge columns: part 1 - evaluation of seismic capacity. Buffalo, New York: NATIONAL CENTER FOR EARTHQUAKE ENGINEERING RESEARCH; 1994.

[30] Menegotto M, Pinto PE. Method of analysis for cyclically loaded R.C. plane frames including changes in geometry and non-elastic behaviour of elements under combined normal force and bending. https://doi.org/10.5169/SEALS-13741; 1973.

[31] Baker JW. Efficient analytical fragility function fitting using dynamic structural analysis. Earthq Spectra 2015;31:579–99. https://doi.org/10.1193/021113EQS025M.

[32] Mangalathu S, Jeon J, DesRoches R. Critical uncertainty parameters influencing seismic performance of bridges using lasso regression. Earthq Eng Struct Dyn 2017;47:784–801. https://doi.org/10.1002/eqe.2991.

[33] Zelaschi C, Monteiro R, Pinho R. Parametric characterization of RC bridges for seismic assessment purposes. Structures 2016;7:14–24. https://doi.org/10.1016/j.istruc.2016.04.003.

[34] Ministero per i lavori pubblici, Norme tecniche per il calcolo, l'esecuzione ed il collaudo delle strutture in cemento armato normale e precompresso e per le strutture metalliche, (1972).

[35] Stefanidou SP, Kappos AJ. Bridge-specific fragility analysis: when is it really necessary? Bull Earthq Eng 2019;17:2245–80. https://doi.org/10.1007/s10518-018-00525-9.

[36] Ministero delle Infrastrutture e dei Trasporti, NTC18, (2018).

[37] CEN. Eurocode 8 - design of structures for earthquake resistence - part 2: bridges. 2025.

[38] Moschonas IF, Kappos AJ, Panetsos P, Papadopoulos V, Makarios T, Thanopoulos P. Seismic fragility curves for Greek bridges: methodology and case studies. Bull Earthq Eng 2008;7:439–68. https://doi.org/10.1007/s10518-008-9077-2.

[39] Manfredi V, Masi A, Özcebe AG, Paolucci R, Smerzini C. Selection and spectral matching of recorded ground motions for seismic fragility analyses. Bull Earthq Eng 2022;20:4961–87. https://doi.org/10.1007/s10518-022-01393-0.

[40] Scott DW. Multivariate density estimation and visualization. In: Gentle JE, Härdle WK, Mori Y, editors. Handb. Comput. Stat. Berlin Heidelberg, Berlin, Heidelberg: Springer; 1992. p. 549–69. https://doi.org/10.1007/978-3-642-21551-3_19.

[41] Dabiri H, Faramarzi A, Dall'Asta A, Tondi E, Micozzi F. A machine learning-based analysis for predicting fragility curve parameters of buildings. J Build Eng 2022;62: 105367. https://doi.org/10.1016/j.jobe.2022.105367.

[42] Mangalathu S, Jeon J-S. Machine learning–based failure mode recognition of circular reinforced concrete bridge columns: comparative study. J Struct Eng 2019; 145:4019104. https://doi.org/10.1061/(ASCE)ST.1943-541X.0002402.

[43] Stefanidou SP, Paraskevopoulos EA, Papanikolaou VK, Kappos AJ. An online platform for bridge-specific fragility analysis of as-built and retrofitted bridges. Bull Earthq Eng 2022;20:1717–37. https://doi.org/10.1007/s10518-021-01299-3.

[44] Wang X, Demartino C, Monti G, Quaranta G, Fiore A. Machine learning-based seismic fragility curves for RC bridge piers. Procedia Struct Integr 2023;44: 1736–43. https://doi.org/10.1016/j.prostr.2023.01.222.

[45] Liu DC, Nocedal J. On the limited memory BFGS method for large scale optimization. Math Program 1989;45:503–28. https://doi.org/10.1007/BF01589116.

[46] Nettis A, Di Mucci VM, Ruggieri S, Uva G. Seismic fragility and risk assessment of isolated bridges subjected to pre-existing ground displacements. Soil Dynam Earthq Eng 2025;194:109335. https://doi.org/10.1016/j.soildyn.2025.109335.